Journal of Thermal Analysis and Calorimetry
https://doi.org/10.1007/s10973-019-08847-9

Effect of phosphate additives on the hydration process of magnesium silicate cements: thermal and spectroscopic characterization

Monica Tonelli[1] · Francesca Martini[2,3] · Alessio Milanesi[1] · Lucia Calucci[2] · Marco Geppi[2,3] · Silvia Borsacchi[2] · Francesca Ridi[1]

Received: 19 July 2019 / Accepted: 15 September 2019

Abstract

The role of phosphate additives on the hydration process of magnesium silicate cement pastes was investigated through a multi-technique approach. A MgO/SiO_2 mixture was hydrated for 28 days either in the absence or in the presence of sodium hexametaphosphate, trimetaphosphate or orthophosphate. Information on the kinetics of the hydration reaction was acquired by monitoring the free water index by means of differential scanning calorimetry, while the hydration products were thoroughly investigated by X-ray diffraction, thermogravimetric analysis, Fourier transform infrared spectroscopy, scanning electron microscopy and ^{29}Si solid-state nuclear magnetic resonance spectroscopy. The overall results provide new insight into the effect of phosphates on the hydration reaction and on the structure of magnesium silicate hydrate cements. All additives showed a plasticizing effect and promoted the formation of the binding phase magnesium silicate hydrate (M–S–H), without significantly altering its structure. Sodium orthophosphate was found to be by far the best-performing additive, even better than sodium hexametaphosphate, which is commonly used in these cementitious formulations. For the first time, ^{31}P solid-state NMR investigation allowed orthophosphate ion to be identified as the effective species.

Keywords Magnesium silicate hydrate · Orthophosphate · Plasticizer · Hydration kinetics · Thermal analysis · MAS NMR

Introduction

Magnesium silicate hydrate (M–S–H) is a colloidal gel obtained by hydration of reactive periclase (MgO) in the presence of silica (SiO_2). Thanks to its cementitious properties, M–S–H represents an environmentally convenient alternative to standard binders based on calcium silicate hydrate (C–S–H) [1, 2]. MgO/SiO_2 cement recently gained considerable attention in the scientific community as it resulted a good candidate for some peculiar applications, such as the cementification of problematic radioactive wastes, enhancing the durability of the deep repositories within the natural clay environment [3–7].

During the hydration of MgO/SiO_2, several reactions can occur: dissolution of MgO to give Mg^{2+} and OH^- ions and precipitation of brucite ($Mg(OH)_2$) when these ions reach the supersaturation point; silica hydration, which in basic conditions brings to the formation of silicate anions;

Monica Tonelli and Francesca Martini have contributed equally to this work.

Electronic supplementary material The online version of this article (https://doi.org/10.1007/s10973-019-08847-9) contains supplementary material, which is available to authorized users.

✉ Silvia Borsacchi
silvia.borsacchi@pi.iccom.cnr.it

✉ Francesca Ridi
francesca.ridi@unifi.it

[1] Department of Chemistry "Ugo Schiff" and CSGI, University of Florence, Via della Lastruccia 3 Sesto Fiorentino, 50019 Florence, Italy

[2] Institute for the Chemistry of OrganoMetallic Compounds, Italian National Council for Research, CNR-ICCOM, via Moruzzi 1, 56124 Pisa, Italy

[3] Department of Chemistry and Industrial Chemistry, University of Pisa, via Moruzzi 13, 56124 Pisa, Italy

Journal : Large 10973 | Dispatch : 19-9-2019 | Pages : 11
Article No. : 8847 | LE | TYPESET
MS Code : JTAC-D-19-01494R1 | CP | DISK

reaction of hydrated silica with Mg^{2+} with formation of M–S–H gel [6–9]. These reactions can be schematized as [6, 9, 10]:

$$MgO + H_2O \rightarrow Mg^{2+} + 2OH^- \leftrightarrow Mg(OH)_2 \quad (1)$$

$$SiO_2 + 2OH^- \rightarrow H_2SiO_4^{2-} \quad (2)$$

$$SiO_2 + OH^- + H_2O \rightarrow H_3SiO_4^- \quad (3)$$

$$3Mg^{2+} + 6OH^- + 2SiO_2 \rightarrow (MgO)_3(SiO_2)_2(H_2O)_2 + H_2O \quad (4)$$

$$3Mg^{2+} + 6OH^- + 4SiO_2 \rightarrow (MgO)_3(SiO_2)_4H_2O + 2H_2O \quad (5)$$

The last two reactions bring to the formation of serpentine and talc, respectively. Indeed, it has been shown that M–S–H is an amorphous phase with a sub-nanometric structure resembling that of Mg-phyllosilicate minerals: depending on the MgO and SiO_2 relative content, their reactivity and the hydration conditions, serpentine-like and/or talc-like nanodomains were found in M–S–H [5, 10, 11].

When preparing cementitious pastes, the addition of admixtures is essential to achieve different goals, such as accelerate or retard setting or hardening, decrease the amount of water needed to obtain a proper workability, improve the mechanical performances and entrain air. For Portland-based cements, many different additives are commonly used to improve specific properties [12–17]. In the field of MgO/SiO_2 cement, sodium hexametaphosphate ($(NaPO_3)_6$, HMP) has been the preferred plasticizer so far [5, 18–20]. Few works reported that the use of about 1–2 wt% of HMP with MgO/SiO_2 produces an effective reduction in the water/solid ratio and an improvement of the cement compressive strength [5, 18, 19]. Walling et al. stated that the addition of HMP does not alter the structure of M–S–H [5], but its role on M–S–H precipitation was not unraveled. Jia et al. investigated the effect of HMP on the hydration of MgO/SiO_2 mixes and the formation of M–S–H [20]. They showed that HMP inhibits the formation of brucite when MgO is hydrated, and hypothesized that this is due to the adsorption of $(6MgOH^+ \cdot (PO_3)_6^{6-})$ complexes on the MgO surface, which prevent the nucleation of $Mg(OH)_2$. The same authors reported that HMP determines a pH increase, which favors silica fume dissolution [21], and, when added in a proper amount, also leads to a rise of Mg^{2+} concentration in solution (the authors speculate the presence of a $[Mg_2(PO_3)_6]^{2-}$ species in solution), enhancing the formation of M–S–H. According to the hypotheses of Jia et al., the hexacycle phosphate molecule is the effective species affecting the properties of MgO/SiO_2 pastes. However, this has not been experimentally demonstrated yet, neither the effect of different phosphate-based additives has been explored so far.

To address these points, in the present work, MgO/SiO_2 pastes were prepared using three different phosphate salts, as shown in Fig. 1: sodium hexametaphosphate ($(NaPO_3)_6$, HMP), sodium trimetaphosphate ($Na_3(PO_3)_3$, TMP) and sodium orthophosphate (Na_3PO_4, OP). The combination of thermal and spectroscopic analyses is often essential to address the full characterization of cementitious materials' properties [22, 23]. In the present work, this multi-technique approach allowed us to obtain a detailed characterization of the samples, clarifying the influence of phosphate additives on the hydration reaction of MgO/SiO_2 mixes and on the formation of M–S–H. In particular, we performed mini-slump tests [24, 25], free water index (FWI) determination (by means of differential scanning calorimetry, DSC) [26–28], pH measurement, X-ray Diffraction (XRD), thermogravimetric analysis (TGA), Fourier transform infrared spectroscopy (FTIR) and scanning electron microscopy (SEM). The effects of the additives on the M–S–H structure were assessed by means of ^{29}Si solid-state nuclear magnetic resonance spectroscopy (SSNMR) and, for the first time, ^{31}P SSNMR was exploited to characterize the phosphate species present in the hydrated samples. The preparation of the specimens was specifically tailored to identify which phosphate species is actually responsible for the improving effects on the hydration reaction. In particular, the additives were not pre-dissolved in water, so to avoid the hydrolysis of the hexacycle and the tricycle before the mixing with MgO and SiO_2 powders.

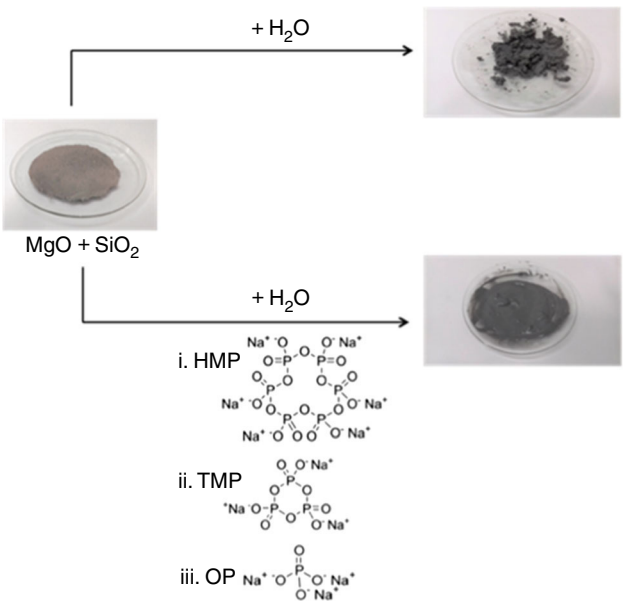

Fig. 1 Scheme of the preparation of MgO/SiO_2 cement paste without (top) and with (bottom) HMP, TMP or OP additives

Journal : Large 10973 | Dispatch : 19-9-2019 | Pages : 11
Article No. : 8847 | LE | TYPESET
MS Code : JTAC-D-19-01494R1 | CP | DISK

Experimental

Materials

Highly reactive MgO (Magnesium oxide N 50, purity ≈ 97%, BET surface area = 150 $m^2\ g^{-1}$) was obtained from Lehmann&Voss&Co., SiO_2 (purity > 90%, BET surface area = 4.33 $m^2\ g^{-1}$) from Elkem. HMP was purchased from CarloErba, TMP and OP from Aldrich.

Samples

Samples were prepared by mixing MgO and SiO_2 in a 1:1 molar ratio (± 0.1). When present, phosphate additives were dry mixed with MgO/SiO_2 at a P:Mg ratio of 0.01 (corresponding to 1 wt% in the case of HMP). Then, the powders were gradually added to milliQ water at a water to solid weight ratio (w/s) of 0.8 and manually mixed. Samples will be indicated throughout the paper as: MSH (without additives), MSH-HMP, MSH-TMP and MSH-OP. The sample labelled as MSH@pH = 11.8 was prepared by dry mixing MgO and SiO_2 and gradually adding the powder to a solution of milliQ water and NaOH at pH = 11.8. The composition of this sample is analogous to MSH, but at same pH established by MSH-OP. For the mini-slump tests, a higher water to solid ratio (w/s = 2) and an automatic mixer were used.

Specimens for TGA, FTIR, SEM, XRD and SSNMR analyses were prepared by stopping the hydration reaction after *n* days (*n*: 1–28): about 1 g of paste was withdrawn, cooled in liquid nitrogen, and freeze-dried (50 mTorr, − 55 °C, 24 h).

Methods

For mini-slump tests, a miniature slump cone was fabricated in PMMA with a top diameter of 19 mm, a bottom diameter of 38 mm and a height of 57 mm, to maintain the same proportion of the slump cone described by ASTM C143 [29]. In the literature, the use of the miniature slump test was reported for Portland cement to compare the performances of water reducing admixtures and to evaluate the workability of the samples [5, 24, 35]. The cone was filled with freshly prepared paste and, after 1 min, lifted with a rapid motion. Thus, the spreading out diameter of the investigated sample was measured [30].

For DSC experiments, roughly 50 mg of each mixed paste was transferred in a steel pan (diameter 7.4 mm, capacity 60 µL) and sealed with a cover equipped with a neoprene O-ring, to avoid water leaking. The pan was maintained at 20 °C, and samples were periodically analyzed in a DSC Q2000 calorimeter from TA Instruments (New Castle, DE, USA), with the following temperature program: equilibrate to − 60 °C, isothermal for 4 min, ramp from − 60 °C to room temperature at 5 °C min^{-1}.

FWI was determined following a procedure already reported in the literature [26, 27]. The method is based on the quantification of free, or freezable, water index by DSC. In this approach, the pastes are periodically frozen and then melted by heating at a constant rate in the DSC, as previously described. The melting peak of free, still unreacted, water is integrated to obtain the melting enthalpy (ΔH_{exp}) and calculate FWI using Eq. (6):

$$FWI = \Delta H_{exp}/\varphi_w \Delta H_{theor} \quad (6)$$

where φ_w is the original weight fraction of water in the paste and ΔH_{theor} is the theoretical value of the melting enthalpy of water (333.4 J g^{-1}).

pH measurements were taken, according to a method already established in the literature [10, 31], using a BASIC 20 CRISON pHmeter calibrated with three buffer solutions at pH 7.00, 9.21 and 10.90 (CRISON), at room temperature (22 ± 1 °C). In a polyethylene flask, 1 g of mixed solid and 10 g of distilled water were added. The container was sealed and constantly shaken in an orbital stirrer. At different time intervals, the solid particles were allowed to settle and the pH of the supernatant was measured.

X-ray diffractograms were recorded with an XRD Bruker New D8 Da Vinci instrument operating at 40 kV and 40 mA, with a Cu source (emitting radiation λ = 1.54 Å). Data were collected in the 5°–70° 2θ range, with an increment of 0.05°, at 0.5 s per step.

TGA measurements were performed by means of a SDT Q600 analyzer from TA Instruments (New Castle, DE, USA) on approximately 10 mg of each sample, in alumina pans, heating from room temperature to 1000 °C at 10 °C min^{-1}, in nitrogen flux (100 ml min^{-1}).

FTIR spectra were acquired with a BioRad FTS-40 spectrometer (Biorad, Cambridge, MA, USA), between 400 and 4000 cm^{-1}, with a resolution of 2 cm^{-1}, accumulating 32 scans. For the analysis, 1 mg of each sample was homogenized with 100 mg of KBr and pressed to obtain a pellet.

SEM images were collected on uncoated fracture surfaces with a field-emission ΣIGMA (Carl Zeiss) microscope, with an accelerating potential of 5 kV.

SSNMR experiments were carried out on a Varian InfinityPlus 400 spectrometer, working at Larmor frequencies of 400.34 MHz, 79.54 MHz and 162.06 MHz for ^{1}H, ^{29}Si and ^{31}P nuclei, respectively, exploiting a CP-MAS probehead accommodating rotors with outer diameter of 7.5 mm. All spectra were obtained using a direct excitation (DE) pulse sequence under high-power decoupling from ^{1}H nuclei and magic-angle spinning (MAS), using air as

Journal : Large 10973 | Dispatch : 19-9-2019 | Pages : 11
Article No. : 8847 | LE | TYPESET
MS Code : JTAC-D-19-01494R1 | CP | DISK

spinning gas and working at room temperature. ^{29}Si DE-MAS spectra were recorded at a MAS frequency of 5.5 kHz, with a recycle delay of 20 s and accumulating 4300 transients. ^{31}P DE-MAS spectra were recorded at MAS frequencies between 4 and 6.2 kHz, accumulating 4–180 transients separated by a recycle delay of 20 s for pristine phosphates and 15,000–40,000 transients with a recycle delay of 5 s for MSH-additive samples. ^{31}P isotropic peaks were identified by comparing spectra recorded at different MAS frequencies. ^{31}P shielding tensors were determined analyzing the spinning sidebands according to the Herzfeld and Berger approach [32], using the HBA software [33]. The Haeberlen convention was used [34], which assigns the principal components σ_{ii} such that $|\sigma_{33} - \sigma^{iso}| > |\sigma_{11} - \sigma^{iso}| \geq |\sigma_{22} - \sigma^{iso}|$, where $\sigma^{iso} = (\sigma_{11} + \sigma_{22} + \sigma_{33})/3$. The shielding anisotropy $\Delta\sigma$ and asymmetry η were calculated as $\Delta\sigma = \sigma_{33} - (\sigma_{11} + \sigma_{22})/2$ and $\eta = (\sigma_{22} - \sigma_{11})/(\sigma_{33} - \sigma^{iso})$. Percentages of the different ^{29}Si and ^{31}P species were obtained from peak areas rescaled on the basis of the respective measured T_1's [10]. The ^{29}Si chemical shift scale was referred to the signal of 3-(trimethylsilyl)-1-propane-sulfonic acid sodium salt at 1.46 ppm. For ^{31}P spectra both the chemical shift and shielding scales were referred to the signal of H_3PO_4 (85%) at 0 ppm.

Results and discussion

HMP is usually added to the MgO/SiO_2 formulations with the aim of improving the fluidity without increasing the water amount. The mini-slump tests performed on the pastes under investigation (see Figure SI1 and Table SI1) show that all the three phosphate additives improve the plasticization, with OP being the most effective one.

The hydration reaction of MgO/SiO_2 was followed in the first 28 days by measuring FWI at different hydration times, to evaluate the influence of the additives on the formation of the M–S–H phase. Figure 2 shows the DSC curves recorded at different hydration times and the FWI versus hydration time profiles of the investigated samples. The decrease in the melting peak of water with time (Fig. 2a) is related to the progress of the hydration reaction, and through the integration of these signals, we calculated the FWI values at each hydration time, thus obtaining the kinetic curves of the process (Fig. 2b). The hydration of all samples shows an induction period in which almost no water reacts (FWI $\approx$ 1), followed by an acceleration period (starting at the induction time, t_i), during which FWI decreases because of the nucleation and growth of the hydrated phases. Then, a change in the curve slope is observed due to the modification of the rate-limiting mechanism, from *nucleation and growth* to *diffusion-limited* behavior, occurring at the diffusion time t_d. The value of FWI at t_d (FWI_d) represents a measurement of the efficiency of the hydration reaction: the lower FWI_d, the higher the water amount used to form hydrated phases during the nucleation-and-growth step [28, 31]. The inset of Fig. 2b illustrates the graphical method used to obtain the t_i, t_d, FWI_d and ΔFWI parameters reported in Table 1. The presence of HMP slightly increases t_i and prolongs the duration of the nucleation-and-growth step, while the addition of TMP does not modify the induction and diffusion times in a significant way with respect to the pristine MSH sample. OP markedly retards the onset of the nucleation and growth period and extends dramatically its duration, t_i and t_d being much longer than for the other samples (Table 1). It is known from the literature, especially in the field of refractory castables [16, 20, 35], that phosphate ions are able to hinder MgO hydration, by easy adsorption on its surface. The long t_i observed in MSH-OP suggests that the interaction of orthophosphate ions with MgO surface is particularly favored in this sample. The FWI_d value is substantially the same for MSH, MSH-HMP and MSH-TMP, which indicates that the efficiency of water consumption during the nucleation-and-growth stage is unaltered by these additives. On the other hand, in the presence of OP, FWI_d is significantly lower, meaning that the hydrated phases keep on precipitating at high rate of formation until $\sim$ 100 h, consuming roughly 40% of the initial water ($FWI_d \sim 0.6$). The experimental values of ΔFWI (Table 1) highlight that OP strongly enhances the hydration reaction during the nucleation-and-growth step.

It was already reported that a high pH enhances M–S–H precipitation by favoring the reactivity of silica. The pH of the investigated samples is shown in the Supplementary Material (Figure SI2). In MSH sample, pH is initially determined by the formation of $Mg(OH)_2$ (pKa $\approx$ 10.5) and then it decreases to $\sim$ 9 because of the consumption of brucite in the reaction with hydrated silica to give M–S–H, as reported in the literature [21, 36, 37]. In the presence of the additives, the trends are similar, but the values of pH are higher over the entire investigated period, especially for MSH-OP. Aqueous solutions of HMP, TMP and OP (with the same concentrations as in the cement pastes) have pH of 5.4, 6.8 and 11.8, respectively. It is worth noting that despite the pH of water solutions of HMP and TMP is lower than the pH of the paste, when these additives are mixed to the cement, the final pH is higher than that of MSH sample and only some tenths of pH unit lower than that of MSH-OP sample. This observation suggests that in the corresponding pastes, HMP and TMP undergo hydrolysis, to some extent. An additional sample "MSH@pH = 11.8" (prepared without any additive, but at the same pH of MSH-OP) was investigated in order to discriminate the effect on the hydration process arising

Journal : Large 10973 | Dispatch : 19-9-2019 | Pages : 11
Article No. : 8847 | LE | TYPESET
MS Code : JTAC-D-19-01494R1 | CP | DISK

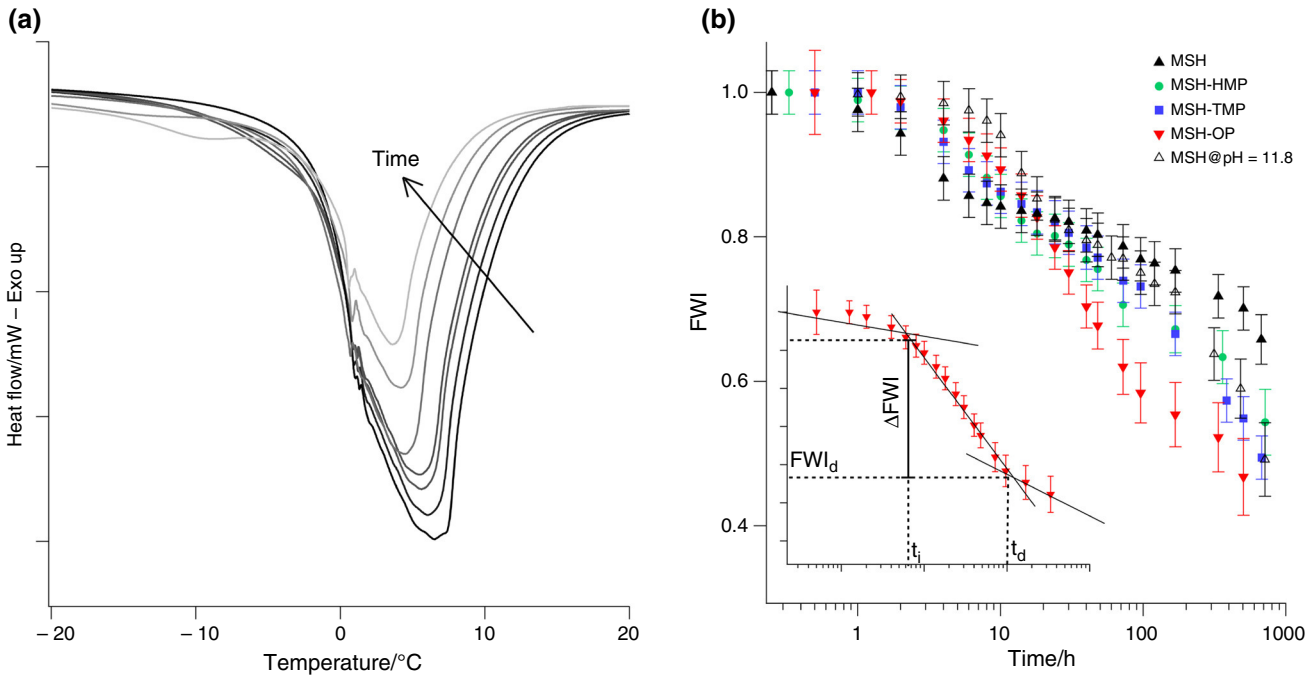

Fig. 2 DSC curves of MSH sample at different hydration times (**a**) and FWI as a function of hydration time for all the investigated samples (**b**)

Table 1 Parameters extracted from the FWI versus hydration time curves as explained in the inset of Fig. 2B

Sample	t_i/h	t_d/h	FWI$_d$ (± 0.05)	ΔFWI (± 0.01)
MSH	1 ± 0.5	6 ± 1	0.85	0.12
MSH-HMP	3 ± 1	18 ± 2	0.80	0.16
MSH-TMP	2 ± 0.5	8 ± 2	0.85	0.11
MSH-OP	6 ± 2	100 ± 10	0.58	0.35
MSH@pH = 11.8	6 ± 2	24 ± 3	0.82	0.12

from the additives from that of pH. Looking at Fig. 2b and Table 1, it is evident that the onset of the nucleation and growth period is strongly retarded in "MSH@pH = 11.8" sample (long t_i), but the efficiency of the reaction is much lower if compared to that of MSH-OP (lower ΔFWI), indicating that the presence of OP strongly affects the efficiency of the hydration reaction.

To obtain information on the effects of the different additives on the composition, morphology and structure of cured pastes, we carried out XRD, TGA, FTIR, SEM and ^{29}Si SSNMR experiments.

In the XRD diffractograms of the investigated samples freeze-dried after 28 days of hydration (Fig. 3), no MgO peaks can be recognized, indicating that MgO completely reacted in the first month. The observed narrow peaks (at 19°, 38°, 51°, 59°, 62° and 68°) are due to brucite, the main crystalline phase of the samples, while the broad peaks at about 23°, 35° and 59° are consistent with the XRD pattern of the amorphous M–S–H phase [20, 38]. In the presence of OP, a low amount of brucite is present, as confirmed by the quantitative estimation performed with the TG analysis reported in Fig. 4.

Figure 4a shows the thermogravimetric profiles of the analyzed samples. The deconvolution of the corresponding differential thermogravimetric (DTG) curves (Fig. 4b) was performed in the 200–800 °C temperature range to quantify the relative amount of brucite in the samples hydrated for 28 days [39–42]. In this region, the well-defined weight loss at about 375 °C (peak #1) is due to the dehydroxylation of $Mg(OH)_2$ [10]. The broad peak observed in the DTG curves (#2) is attributed to multiple weight losses: M–S–H silanols, hydroxyl groups and strongly adsorbed water of the gel phase [10, 11]. For this reason, it cannot be used for a quantitative estimation of the binder phase. However, it is clear that the relative amount of brucite in MSH-OP is significantly lower than in the other samples (Table 2). Considering that the FWI data revealed that OP increases the amount of "hydrated phases" and that DTG and XRD results show a very low amount of brucite in MSH-OP, we can infer that the presence of orthophosphate enhances the formation of the M–S–H gel.

Journal : Large 10973 Dispatch : 19-9-2019 Pages : 11
Article No. : 8847 LE TYPESET
MS Code : JTAC-D-19-01494R1 CP DISK

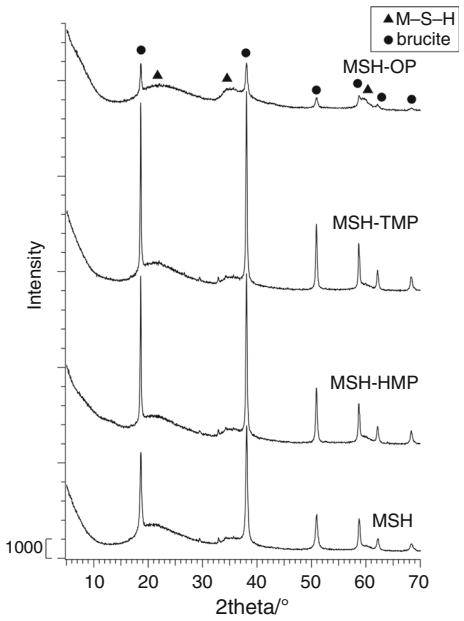

Fig. 3 XRD diffractograms of the investigated samples freeze-dried after 28 days of hydration

The evolution with time of the hydrated phases was also followed by means of FTIR spectroscopy. Figure 5 reports the FTIR spectra in the 3900–2500 cm^{-1} range, which is particularly informative because it includes the frequencies of the OH vibrations [43]. As expected from the literature for the hydration of MgO and SiO_2 [11, 44], all samples show the sharp Mg-OH stretching vibration of brucite at 3696 cm^{-1} and the OH vibrations attributed to the structural hydroxyl groups of the M–S–H phase at 3300 cm^{-1}. The signal at 3300 cm^{-1} increases with time in all samples, confirming the formation of the binder gel phase. In the presence of OP, this signal is particularly intense, confirming the enhancement of M–S–H precipitation disclosed by FWI and TG/DTG results. In all the samples, the amount of brucite decreases as time increases, because of its consumption in the reaction with silica to form M–S–H.

The SEM images (Fig. 6) show the heterogeneous complex morphology of the samples. It is possible to recognize the spherical shape of unreacted silica particles, the amorphous morphology of M–S–H and brucite platelets [10, 45]. Interestingly, in the MSH-OP sample, many spherical holes were identified. (One of them is displayed in the zoom.) Their presence is the clear demonstration that silica acts as a "mold" for M–S–H formation, occurring by the dissolution and re-precipitation process previously hypothesized in the literature [46–48].

A clear picture of the structure of the amorphous silicate phases present in the samples after 28 days of hydration is provided by ^{29}Si SSNMR spectra (Fig. 7). The spectrum of MSH shows the typical signals of the M–S–H phase, whose structure at the sub-nanometric scale is known to resemble that of magnesium phyllo-silicates [5, 10, 37, 38]. It is

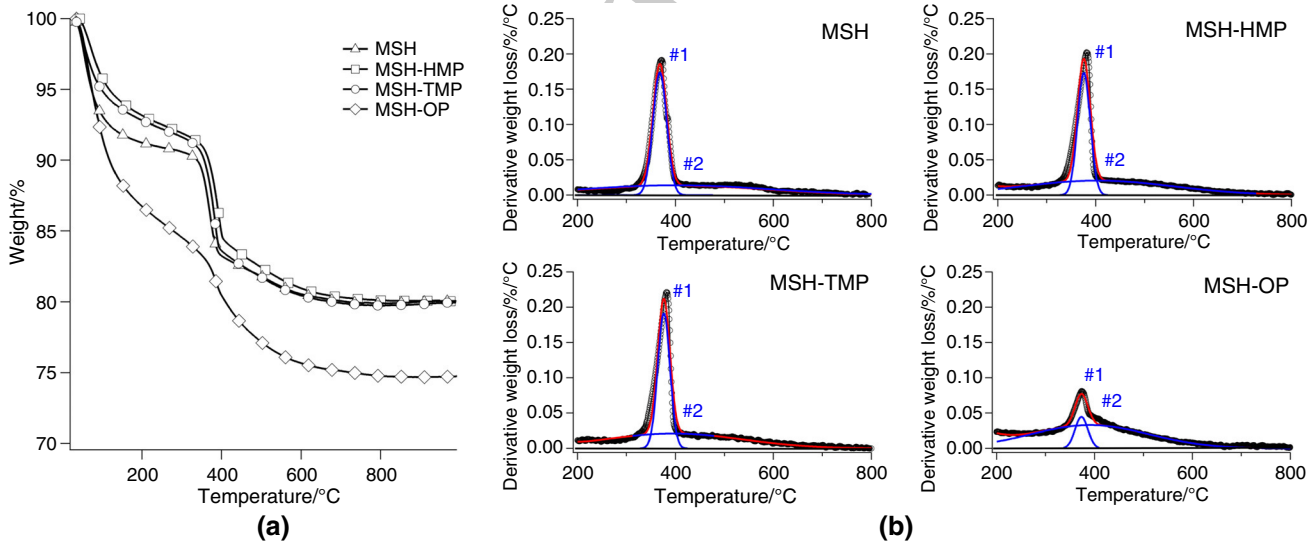

Fig. 4 TG curves (**a**) and deconvolution of the DTG curves (**b**) of the samples freeze-dried after 28 days of hydration. Black markers represent the experimental data; red lines are the global fitting curves; blue lines are the Gaussian peaks obtained by the fitting procedure

Table 2 Position and percentage area of the Gaussian peak #1 resulting from the deconvolution of DTG curves

	MSH	MSH	MSH-HMP	MSH-TMP	MSH-OP
Peak 1	T_{max}/ °C	374 ± 1	376 ± 1	376 ± 1	373 ± 1
	Area/%	6.6 ± 0.1	5.6 ± 0.1	6.0 ± 0.1	1.5 ± 0.1

Journal : Large 10973 Dispatch : 19-9-2019 Pages : 11
Article No. : 8847
MS Code : JTAC-D-19-01494R1
☐ LE ☑ CP ☐ TYPESET ☑ DISK

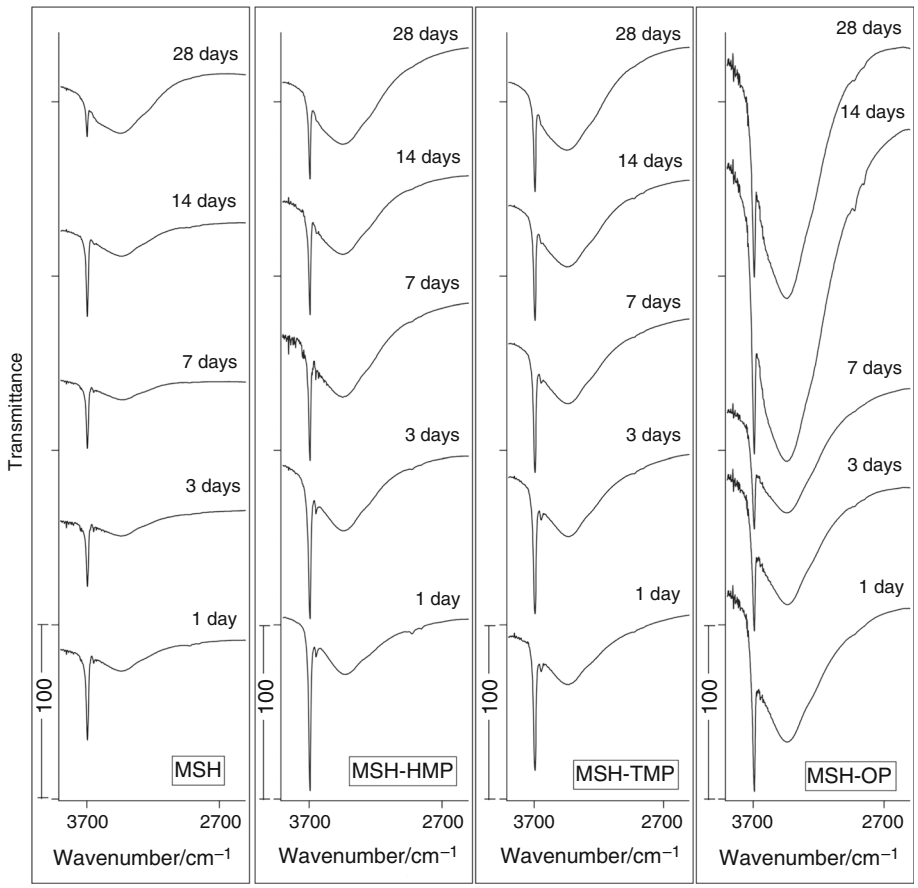

Fig. 5 FTIR spectra of the investigated samples at different hydration times in the 3900–2500 cm^{-1} spectral range. Curves have been offset for the sake of clarity

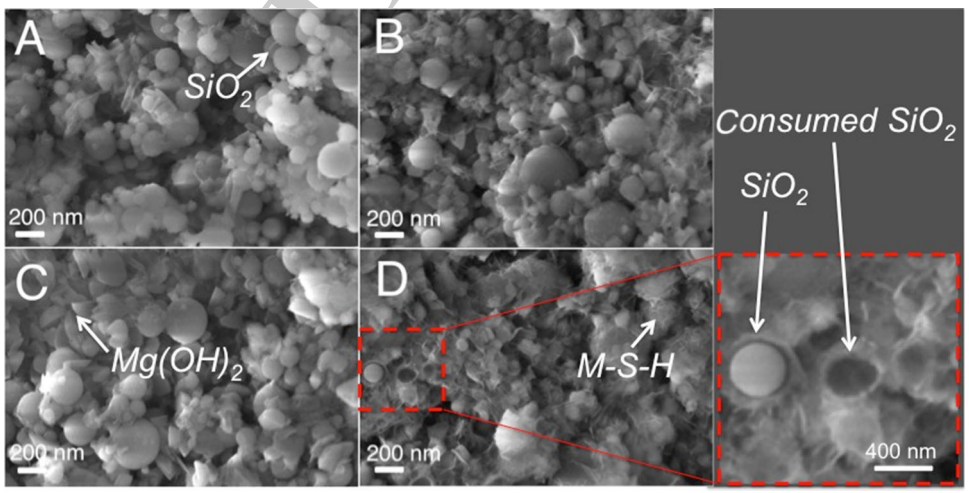

Fig. 6 SEM images (magnification: 120 K X) of samples freeze-dried after 28 days of hydration: **a** MSH; **b** MSH-HMP; **c** MSH-TMP; **d** MSH-OP

possible to recognize signals of Q^3 (Si(OMg)$(OSi)_3$), Q^2 (Si(OMg)$(OSi)_2OH$) and Q^1 (Si(OMg)(OSi)$(OH)_2$) sites at about − 92, − 85 and − 80 ppm, respectively [10, 38]. It is worth noticing that, differently from M–S–H previously obtained [5, 10, 38, 44], which showed two or more distinct Q^3 signals ascribed to serpentine- and talc-like structures, here a sole Q^3 signal is observed with a chemical shift typical of serpentines. Moreover, an intense broad signal ascribable to unreacted silica is present in the spectra at about − 111 ppm. The relatively scarce reactivity of silica can explain the preferential formation of serpentine domains for which the Si:Mg ratio is lower than in talc (2:3 vs. 4:3). Samples prepared with additives show the same signals as MSH, although with different relative intensities.

From the relative amounts of the different silicon species (Table 3), indicated as "Q^i" and "silica" in Eqs. 7 and

Journal : Large 10973 Dispatch : 19-9-2019 Pages : 11
Article No. : 8847 LE TYPESET
MS Code : JTAC-D-19-01494R1 CP DISK

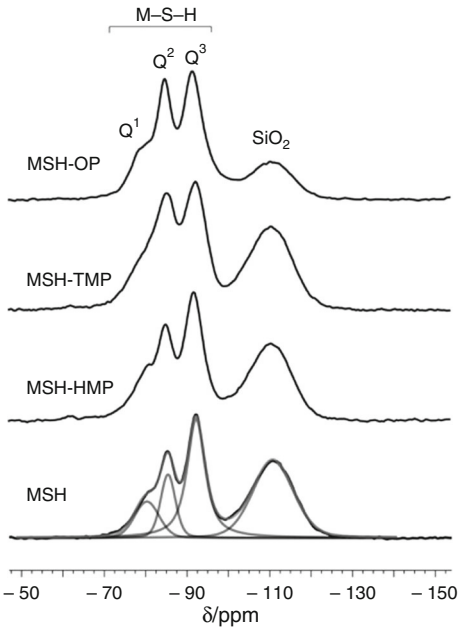

Fig. 7 ^{29}Si DE-MAS spectra of the indicated samples after 28 days of hydration. The peak assignment to different silicon species is reported on the spectrum of MSH-OP. For MSH, the spectral deconvolution is also shown in gray

8, it is possible to calculate the silica reaction degree (RD) and the condensation degree (CD) of M–S–H as [10]:

$$\mathrm{RD} = 100 \times \left(Q^1 + Q^2 + Q^3\right)/\left(Q^1 + Q^2 + Q^3 + \mathrm{silica}\right) \quad (7)$$

$$\mathrm{CD} = 100 \times \left(3Q^3 + 2Q^2 + Q^1\right)/3\left(Q^3 + Q^2 + Q^1\right) \quad (8)$$

Values of RD (Table 3) confirm and quantify the indications obtained from the other characterization techniques on the enhanced formation of M–S–H in the presence of phosphates: OP has the strongest effect, increasing by ~ 30% the amount of reacted silica, while HMP and TMP determine smaller and similar increases (2–7%). On the other hand, the comparison between the CD values obtained in the presence and in the absence of additives indicates that they do not substantially modify the structure of M–S–H: In all cases, M–S–H with a serpentine-like sub-nanometric structure is obtained, with a slightly lower CD in the presence of TMP and a slightly higher one in the presence of HMP and OP.

In order to clarify the different effects of the investigated additives, we carried out a detailed analysis of the phosphorus containing species present in the samples by means of ^{31}P SSNMR. The analysis was extended also to the pristine additives, to better highlight the chemical and structural modifications they underwent during the hydration of MgO/SiO_2. All the ^{31}P DE-MAS spectra (shown in Fig. 8) were analyzed to obtain, for each phosphorous species, the isotropic chemical shift (δ^{iso}), the shielding tensor and the relative amount (Table 4).

The spectrum of OP, in agreement with the literature [34, 49, 50], shows only one signal with isotropic chemical shift of 7.7 ppm and very weak first-order spinning sidebands. These features are determined by the high symmetry of the local electronic environment of phosphorus nuclei in the orthophosphate (PO_4^{3-}) groups. In a commonly accepted nomenclature, according to which phosphorus nuclei in phosphate moieties are denoted with Q^n, where n is the number of P-O-P bonds, only Q^0 sites are present in OP. The spectra of TMP and HMP show several signals with quite broad spinning sideband patterns. In particular, TMP displays three narrow signals with δ^{iso} of − 15.8, − 18.5, − 19.5 ppm and quite similar shielding tensors (Table 4), due to Q^2 sites of the TMP rings. The presence of three different signals was already reported in the literature and attributed to either inequivalent sites in the crystals or multiple solid forms [34]. Very weak and broad signals with δ^{iso} of about − 5 and + 5 ppm are ascribable to impurities. The spectrum of HMP shows three signals at δ^{iso} of 2.5, − 7.6 and − 19.5 ppm. Peaks are broad, in agreement with the amorphous character of HMP, and show quite different spinning sideband patterns. The signal

Table 3 Percentages (I) and isotropic chemical shift values (δ^{iso}) of the different silicon species in the ^{29}Si SSNMR spectra

Silicon species	δ^{iso}/ppm[a]	I/%			
		MSH	MSH-HMP	MSH-TMP	MSH-OP
Q^1	− 80.2	9	8	13	12
Q^2	− 85.2	10	6	15	13
Q^3	− 92.0	31	37	29	51
Silica	− 111.0	50	49	43	24
RD/%[b]		50	52	57	76
CD/%[b]		81	85	76	84

Values of RD and CD, obtained by Eqs. 7 and 8, are also reported

[a]± 0.2 ppm

[b]± 2%

Journal : Large 10973 Dispatch : 19-9-2019 Pages : 11
Article No. : 8847 LE TYPESET
MS Code : JTAC-D-19-01494R1 CP DISK

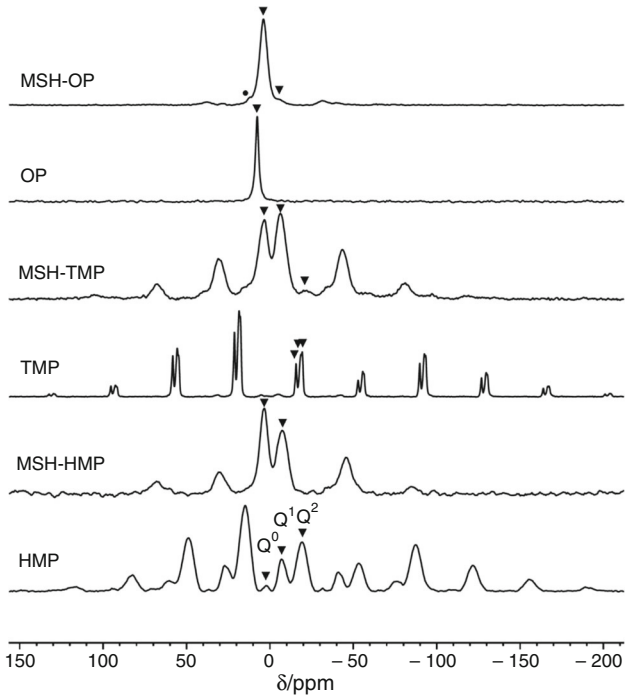

Fig. 8 ^{31}P DE-MAS spectra of pristine additives and MSH-additive samples, as indicated in the figure. Isotropic signals are marked with full triangles, and the peak assignment to Q^i phosphorus species is indicated in the spectrum of HMP. The full circle indicates a weak signal at about 12 ppm ascribable to anhydrous OP [47]

at − 19.5 ppm, characterized by the largest shielding anisotropy, arises from Q^2 sites of HMP rings [49]. The other two peaks (2.5 and − 7.6 ppm, accounting for about 17% of phosphorus nuclei in the sample) can be ascribed to Q^0 and Q^1 sites of orthophosphate and pyrophosphate ($P_2O_7^{4-}$) moieties, respectively, present as impurities in the sample.

The ^{31}P spectra of MSH-additive samples show two signals with δ^{iso} of about 4 and − 7 ppm, although with quite different relative intensities. For MSH-TMP a weak Q^2 signal (δ^{iso} = − 22 ppm) is also detected. On the basis of the values of δ^{iso} and shielding tensors, the main signals can be ascribed to hydrated orthophosphate (Q^0) and pyrophosphate (Q^1) anions [39, 49]. The hydrated environments can be envisaged as water included in the solids or OH groups of M–S–H. In analogy to what already reported for orthophosphate ions in calcium silicate hydrate [51], it is possible that phosphate ions interact with the layers of the M–S–H structure. Moreover, the presence of amorphous magnesium orthophosphates cannot be ruled out [50, 52]. The comparison between the spectra of MSH-additives and those of pristine additives unambiguously highlights that, during cement hydration, the most condensed metaphosphate species (Q^2) present in HMP and TMP rings almost completely dissociate into ortho- and pyrophosphate (Q^0 and Q^1) ions, due to the alkaline pH [53, 54]. Signal intensities (Fig. 8 and Table 4) indicate that the amount of orthophosphate species decreases in the order MSH-OP > MSH-HMP > MSH-TMP, while pyrophosphates are most abundant in MSH-TMP.

All this considered, these results clearly demonstrate that there is a strong correspondence between higher amount of orthophosphate ions available during cement hydration and better additive performances, in terms of retarding and plasticizing effects and efficiency of M–S–H formation. This can be ascribed to the combination of the following factors: the favored interaction between orthophosphate ions and MgO surface, the increased

Table 4 Isotropic chemical shifts (δ^{iso}), percentages (I) and parameters of the shielding tensors of the ^{31}P species in pristine additives and MSH-additive samples

Sample	Q^n	δ^{iso}/ppm	I/%	σ_{11}/ppm	σ_{22}/ppm	σ_{33}/ppm	$\Delta\sigma$/ppm	η
OP	Q^0	7.7	100	ND[a]	ND	ND	ND	ND
TMP	Q^2	− 15.8	36	− 90	− 38	175	239	0.33
	Q^2	− 18.5	46	− 82	− 35	173	232	0.31
	Q^2	− 19.5	18	− 101	− 13	173.0	230	0.57
HMP	Q^0	2.5	<1	ND	ND	ND	ND	ND
	Q^1	− 7.6	17	− 68	− 1	92	127	0.80
	Q^2	− 19.5	83	− 90	− 23	172	229	0.44
MSH-OP	Q^0	3.9	95	ND	ND	ND	ND	ND
	Q^1	− 5.2	5	ND	ND	ND	ND	ND
MSH-TMP	Q^0	3.9	21	ND	ND	ND	ND	ND
	Q^1	− 6.6	72	83	14	− 76	− 125	0.83
	Q^2	− 22.0	7	ND	ND	ND	ND	ND
MSH-HMP	Q^0	3.8	38	ND	ND	ND	ND	ND
	Q^1	− 7.6	62	72	24	− 73	− 121	0.60

[a]Shielding tensors could not be determined for signals showing very low intensity or few spinning sidebands

Journal : Large 10973 Dispatch : 19-9-2019 Pages : 11
Article No. : 8847 LE TYPESET
MS Code : JTAC-D-19-01494R1 CP DISK

availability of Mg^{2+} ions in solution, and the higher silica reactivity. In conclusion, orthophosphate ion was identified as the most active species, and thus OP as the best-performing additive.

Conclusions

In this study, the effects on the formation and structure of M–S–H have been assessed for three phosphate salts: HMP, already used as plasticizer in MgO/SiO_2 cement pastes, TMP and OP, here explored for the first time. By means of a combined thermal and spectroscopic analyses, we found that all the tested additives increase the fluidity of the pastes and enhance the formation of M–S–H, inducing minor modifications on its structure. In particular, the free water index versus time curves, obtained by DSC measurements, allowed us to assess the hydration kinetics of pastes prepared with the different additives, evidencing that OP is the most efficient one in enhancing the formation of hydrated phases. The results of TGA, XRD, FTIR and ^{29}Si SSNMR experiments demonstrated in particular that the formation of M–S–H is strongly increased by the presence of OP. The detailed analysis of the phosphorus species in the pastes, here performed for the first time by means of ^{31}P SSNMR, highlighted that the condensed phosphate additives undergo hydrolysis, giving rise to ortho- and pyrophosphate species. A clear correspondence was found between additive best performances and highest amount of orthophosphate ions, making us to conclude that these are the species really responsible for the enhancement of M–S–H formation.

As a consequence of our investigation, we propose that OP could substitute HMP as a plasticizer of MgO/SiO_2 cement, since its performances are clearly better and its use does not imply cost drawback.

Acknowledgements This work was supported by Ministero dell'Istruzione, Università e Ricerca scientifica—MIUR (FIR2013 Project RBFR132WSM). The CSGI Consortium is gratefully acknowledged.

References

1. Flatt RJ, Roussel N, Cheeseman CR. Concrete: an eco material that needs to be improved. J Eur Ceram Soc. 2012;32:2787–98. https://doi.org/10.1016/j.jeurceramsoc.2011.11.012.
2. Walling SA, Provis JL. Magnesia-based cements: a journey of 150 years, and cements for the future? Chem Rev. 2016;16:4170–204. https://doi.org/10.1021/acs.chemrev.5b00463.
3. Dauzeres A, Achiedo G, Nied D, Bernard E, Alahrache S, Lothenbach B. Magnesium perturbation in low-pH concretes placed in clayey environment—solid characterizations and modeling. Cem Concr Res. 2016;79:137–50. https://doi.org/10.1016/j.cemconres.2015.09.002.
4. Garciá Calvo JL, Hidalgo A, Alonso C, Fernández Luco L. Development of low-pH cementitious materials for HLRW repositories: resistance against ground waters aggression. Cem Concr Res. 2010;40:1290–7. https://doi.org/10.1016/j.cemconres.2009.11.008.
5. Walling SA, Kinoshita H, Bernal SA, Collier NC, Provis JL. Structure and properties of binder gels formed in the system $Mg(OH)_2$–SiO_2–H_2O for immobilisation of Magnox sludge. Dalton Trans. 2015;44:8126–37. https://doi.org/10.1039/C5DT00877H.
6. Zhang T, Cheeseman CR, Vandeperre LJ. Development of low pH cement systems forming magnesium silicate hydrate (M–S–H). Cem Concr Res. 2011;41:439–42. https://doi.org/10.1016/j.cemconres.2011.01.016.
7. Zhang T, Vandeperre LJ, Cheeseman CR. Development of magnesium silicate hydrate cement system for nuclear waste encapsulation. In: NUWCEM, Avignon; 2011. p. 582–591.
8. Szczerba J, Prorok R, Sniezek E, Madej D, Maslona K. Influence of time and temperature on ageing and phases synthesis in the MgO–SiO_2–H_2O system. Thermochim Acta. 2013;567:57–64. https://doi.org/10.1016/j.tca.2013.01.018.
9. Li Z, Zhang T, Hu J, Tang Y, Niu Y, Wei J, Yu Q. Characterization of reaction products and reaction process of MgO–SiO_2–H_2O system at room temperature. Constr Build Mater. 2014;61:252–9. https://doi.org/10.1016/j.conbuildmat.2014.03.004.
10. Tonelli M, Martini F, Calucci L, Fratini E, Geppi M, Ridi F, Borsacchi S, Baglioni P. Structural characterization of magnesium silicate hydrate: towards the design of eco-sustainable cements. Dalton Trans. 2016;45:3294–304. https://doi.org/10.1039/C5DT03545G.
11. Nied D, Enemark-Rasmussen K, L'Hopital E, Skibsted J, Lothenbach B. Properties of magnesium silicate hydrates (M–S–H). Cem Concr Res. 2016;79:323–32. https://doi.org/10.1016/j.cemconres.2015.10.003.
12. Taylor HFW. Cement Chemistry. 2nd ed. London: Thomas Telford; 1997.
13. Plank J, Sakai E, Miao CW, Yu C, Hong JX. Chemical admixtures—chemistry, applications and their impact on concrete microstructure and durability. Cem Concr Res. 2015;78:81–99. https://doi.org/10.1016/j.cemconres.2015.05.016.
14. Bénard P, Garrault S, Nonat A, Cau-dit-Coumes C. Hydration process and rheological properties of cement pastes modified by orthophosphate addition. J Eur Ceram Soc. 2005;25:1877–83. https://doi.org/10.1016/j.jeurceramsoc.2004.06.017.
15. Bénard P, Garrault S, Nonat A, Cau-dit-Coumes C. Influence of orthophosphate ions on the dissolution of tricalcium silicate. Cem Concr Res. 2008;38:1137–41. https://doi.org/10.1016/j.cemconres.2008.03.019.
16. Ltifi M, Guefrech A, Mounanga P. Effects of sodium tripolyphosphate addition on early-age physico-chemical properties of cement pastes. Procedia Eng. 2011;10:1457–62. https://doi.org/10.1016/j.proeng.2011.04.242.
17. Wang X, Zhang J, Yang Y, et al. Effect of side chains in block polycarboxylate superplasticizers on early-age properties of cement paste. J Therm Anal Calorim. 2018;133:1439. https://doi.org/10.1007/s10973-018-7231-x.
18. Zhang T, Vandeperre LJ, Cheeseman CR. Formation of magnesium silicate hydrate (M–S–H) cement pastes using sodium hexametaphosphate. Cem Concr Res. 2014;65:8–14. https://doi.org/10.1016/j.cemconres.2014.07.001.
19. Wei J, Yu Q, Zhang W, Zhang H. Reaction products of MgO and microsilica cementitious materials at different temperatures. J Wuhan Univ Technol-Mater Sci Ed. 2011;26:745–8. https://doi.org/10.1007/s11595-011-0304-3.
20. Jia Y, Wang B, Wu Z, Han J, Zhang T, Vandeperre LJ, Cheeseman CR. Role of sodium hexametaphosphate in MgO/SiO_2 cement pastes. Cem Concr Res. 2016;89:63–71. https://doi.org/10.1016/j.cemconres.2016.08.003.

Journal : Large 10973 | Dispatch : 19-9-2019 | Pages : 11
Article No. : 8847 | ☐ LE | ☐ TYPESET
MS Code : JTAC-D-19-01494R1 | ☑ CP | ☑ DISK

21. Jin F, Al-Tabbaa A. Strength and hydration products of reactive MgO–silica pastes. Cem Concr Compos. 2014;52:27–33. https://doi.org/10.1016/j.cemconcomp.2014.04.003.
22. Romano RC, Bernardo HM, Maciel MH, et al. Using isothermal calorimetry, X-ray diffraction, thermogravimetry and FTIR to monitor the hydration reaction of Portland cements associated with red mud as a supplementary material. J Therm Anal Calorim. 2019;137:1877–90. https://doi.org/10.1007/s10973-019-08095-x.
23. Mokhtari A, Belhouchet H, Guermat A. In situ high-temperature X-ray diffraction, FT-IR and thermal analysis studies of the reaction between natural hydroxyapatite and aluminum powder. J Therm Anal Calorim. 2019;136:1515–26. https://doi.org/10.1007/s10973-018-7812-8.
24. Kantro DL. Influence of water-reducing admixtures on properties of cement paste—a miniature slump test. Cem Concr Aggreg. 1980;2:95–102. https://doi.org/10.1520/CCA10190J.
25. Roussel N, Stefani C, Leroy R. From mini-cone test to Abrams cone test: measurement of cement-based materials yield stress using slump tests. Cem Concr Res. 2005;35:817–22. https://doi.org/10.1016/j.cemconres.2004.07.032.
26. Damasceni A, Dei L, Fratini E, Ridi F, Chen S–H, Baglioni P. A novel approach based on differential scanning calorimetry applied to the study of tricalcium silicate hydration kinetics. J Phys Chem B. 2002;106:11572–8. https://doi.org/10.1021/jp020211l.
27. Ridi F, Dei L, Fratini E, Chen S–H, Baglioni P. Hydration kinetics of tri-calcium silicate in the presence of superplasticizers. J Phys Chem B. 2003;107:1056–61. https://doi.org/10.1021/jp027346b.
28. Ridi F, Fratini E, Luciani P, Winnefeld F, Baglioni P. Hydration kinetics of tricalcium silicate by calorimetric methods. J Colloid Interface Sci. 2011;364:118–24. https://doi.org/10.1016/j.jcis.2011.08.010.
29. Flick EW. Handbook of adhesives raw materials. 2nd ed. New York: William Andrew; 1989.
30. Mebrouki A, Belas N, Bendani K, Bouhamou N. A self-compacting cement paste formulation using mixture design. J Appl Sci. 2009;9:4127–36. https://doi.org/10.3923/jas.2009.4127.4136.
31. Tonelli M, Martini F, Calucci L, Geppi M, Borsacchi S, Ridi F. Traditional Portland cement and MgO-based cement: a promising combination? Phys Chem Earth Parts A/B/C. 2017;99:158–67. https://doi.org/10.1016/j.pce.2017.01.011.
32. Herzfeld J, Berger AE. Sideband intensities in NMR spectra of samples spinning at the magic angle. J Chem Phys. 1980;73:6021–30. https://doi.org/10.1063/1.440136.
33. Eichele K, Wasylishen RE. HBA: Herzfeld–Berger analysis program, 2001. http://www.ccp14.ac.uk/ccp/web-mirrors/klaus_eichele_software/klaus/hba.html#general. Accessed 23 Aug 2019.
34. Griffiths L, Root A, Harris R, Packer K, Chippendale A, Tromans F. Magic-angle spinning P-31 nuclear-magnetic-resonance of polycrystalline sodium phosphates. J Chem Soc-Dalton Trans. 1986;10:2247–51. https://doi.org/10.1039/DT9860002247.
35. Souza TM, Luz AP, Santos T Jr, Gimenes DC, Miglioli MM, Correa AM, Pandolfelli VC. Phosphate chemical binder as an anti-hydration additive for Al_2O_3–MgO refractory castables. Ceram Int. 2014;40:1503–12. https://doi.org/10.1016/j.ceramint.2013.07.035.
36. Schneider M, Romer M, Tschudin M, Bolio H. Sustainable cement production—present and future. Cem Concr Res. 2011;41:642–50. https://doi.org/10.1016/j.cemconres.2011.03.019.
37. Jin F, Al-Tabbaa A. Thermogravimetric study on the hydration of reactive magnesia and silica mixture at room temperature. Thermochim Acta. 2013;566:162–8. https://doi.org/10.1016/j.tca.2013.05.036.
38. Martini F, Tonelli M, Geppi M, Ridi F, Borsacchi S, Calucci L. Hydration of MgO/SiO_2 and Portland cement mixtures: a structural investigation of the hydrated phases by means of X-ray diffraction and solid state NMR spectroscopy. Cem Concr Res. 2017;102:60–7. https://doi.org/10.1016/j.cemconres.2017.08.029.
39. Gabbott P. Principles and applications of thermal analysis. Blackwell Pub: Hoboken; 2008. p. 107.
40. Mendoza O, Sierra G, Tobón JI. Effect of the reagglomeration process of multi-walled carbon nanotubes dispersions on the early activity of nanosilica in cement composites. Constr Build Mater. 2014;54:550–7. https://doi.org/10.1016/j.conbuildmat.2013.12.084.
41. Dweck J, Ferreira da Silva PF, Büchler PM, Cartledge FK. Study by thermogravimetry of the evolution of ettringite phase during type II Portland cement hydration. J Therm Anal Calorim. 2002;69:179–86. https://doi.org/10.1023/A:1019950126184.
42. Guirado F, Galí S, Chinchón JS. Thermal decomposition of hydrated alumina cement. Cem Concr Res. 1998;28:381–90. https://doi.org/10.1016/S0008-8846(98)00007-6.
43. Catauro M, Bollino F, Papale F, Gallicchio M, Pacifico S. Synthesis and chemical characterization of new silica polyethylene glycol hybrid nanocomposite materials for controlled drug delivery. J Drug Deliv Sci Tec. 2014;24(4):320–5. https://doi.org/10.1016/S1773-2247(14)50069-X.
44. Lothenbach B, Nied D, L'Hôpital E, Achiedo G, Dauzères A. Magnesium and calcium silicate hydrates. Cem Concr Res. 2015;77:60–8. https://doi.org/10.1016/j.cemconres.2015.06.007.
45. Tran HM, Scott A. Strength and workability of magnesium silicate hydrate binder systems. Constr Build Mater. 2017;131:526–35. https://doi.org/10.1016/j.conbuildmat.2016.11.109.
46. Martini F, Borsacchi S, Geppi M, Tonelli M, Ridi F, Calucci L. Monitoring the hydration of MgO-based cement and its mixtures with Portland cement by ^{1}H NMR relaxometry. Micropor Mesopor Mater. 2018;269:26–30. https://doi.org/10.1016/j.micromeso.2017.05.031.
47. Chen J, Li T, Li X, Chou K-C, Hou X. Some new perspective on the reaction mechanism of MgO–SiO_2–H_2O system. Int J Appl Ceram Technol. 2016;13:1164–72. https://doi.org/10.1111/ijac.12607.
48. Martini F, Borsacchi S, Geppi M, Forte C, Calucci L. Hydration of MgO-based cement: water dynamics by 1H fast field-cycling NMR relaxometry. J Phys Chem C. 2017;121:26851–9. https://doi.org/10.1021/acs.jpcc.7b09154.
49. Hayashi S, Hayamizu K. High-resolution solid-state ^{31}P NMR of alkali phosphates. Bull Chem Soc Jpn. 1989;62:3061–8. https://doi.org/10.1246/bcsj.62.3061.
50. Turner GL, Smith KA, Kirkpatrick RJ, Oldfieldt E. Structure and cation effects on phosphorus-31 NMR chemical shifts and chemical-shift anisotropies of orthophosphates. J Magn Reson. 1986;70:408–15. https://doi.org/10.1016/0022-2364(86)90129-0.
51. Poulsen SL, Jakobsen HJ, Skibsted J. Incorporation of phosphorus guest ions in the calcium silicate phases of Portland cement from ^{31}P MAS NMR spectroscopy. Inorg Chem. 2010;49:5522–9. https://doi.org/10.1021/ic100140j.
52. Weber J, Auf der Günne JS. Calculation of NMR parameters in ionic solids by an improved self-consistent embedded cluster method. Phys Chem Chem Phys. 2009;12:583–603. https://doi.org/10.1039/B909870D.
53. Morgen RA, Swoope RL. The useful life of pyro-, meta-, and tetraphosphates. Ind Eng Chem. 1943;35:821–4. https://doi.org/10.1021/ie50403a021.
54. Bell RN. Hydrolysis of dehydrated sodium phosphates. Ind Eng Chem. 1947;39:136–40. https://doi.org/10.1021/ie50446a013.

Journal : Large 10973 | Dispatch : 19-9-2019 | Pages : 11
Article No. : 8847 | ☐ LE | ☐ TYPESET
MS Code : JTAC-D-19-01494R1 | ☑ CP | ☑ DISK